J Therm Anal Calorim (2011) 103:185–193
DOI 10.1007/s10973-010-1059-3

Low temperature reactivity in agglomerates containing iron oxide

Studies in the $Ca(OH)_2$–C–Fe_2O_3 system

Ryan Robinson · Fabrice Patisson · Bo Björkman

Received: 9 October 2009 / Accepted: 14 September 2010 / Published online: 16 October 2010

Abstract In this study, we have attempted to explain the complex reactions that occur during the dehydration of $Ca(OH)_2$, in the presence of solid carbon and Fe_2O_3, in order to clarify their role as eventual precursors to the reduction and high temperature strength characteristics in feedstock agglomerates of iron and steelmaking by-products. A series of simultaneous thermo-gravimetric (TG), differential thermal analytic (DTA), and mass spectrometric (MS) tests were performed on agglomerated sample mixes of $Ca(OH)_2$, C, and Fe_2O_3 to test the influence of heating rate and particle size on the transformations occurring below 1,073 K in inert atmosphere. The overall transformation begins with calcium hydroxide dehydration. Nucleation and growth of CaO grains during dehydration, as well as subsequent gasification of solid carbon, are highly dependent on the governing interstitial particle porosity and mildly dependent on the heating rate in and around agglomerates. The reduction of hematite in current agglomerates is, by association to preceding reactions, partly dependent on porosity and heating rate, but the mechanism of reduction was also found to be highly dependent on the particle size of iron oxides. Furthermore, in areas of intimate contact between CaO and iron oxide, a calcium ferrite phase appears in the form of angular and calcium-rich particles.

Keywords Iron oxide reduction · Carbon gasification · Simultaneous TG/DTA/MS · Kinetic analysis

R. Robinson (✉) · B. Björkman
Luleå University of Technology, 97187 Luleå, Sweden
e-mail: ryro@ltu.se

F. Patisson
LSG2M, Nancy-Université, Parc de Saurupt, CS 14234,
54042 Nancy Cedex, France

Introduction

Worldwide, iron and steelmaking facilities generate between 30 and 40 million tons of by-product dusts that are feasible for recycling [1]. The recycling and utilization of by-product agglomerates containing these dusts have shown to result in several industrial benefits, mostly in the decrease of natural resource dependence, reduction of landfill, and indirectly as energy savings [2]. These by-product dusts contain considerable amounts of iron oxides, hydrated lime, and carbon [3, 4], a chemistry that is suitable for preparation of self-reducing/self-fluxing agglomerates. The inherent chemistry and proximity of reactants in self-reducing by-product agglomerates also gives a technical advantage as the rate of reaction is high resulting in a process with high productivity [5]. Therefore, a good understanding of the self-reduction characteristics is essential for further development of cold-bonded agglomerates containing by-products for use as recycle in the steelmaking industry. In recent decades, many researchers have studied the reduction behavior of composites containing various assemblages of iron oxide and carbon. Mantovani and Takano have reported that the reduction of self-reducing pellets containing a mixture of EAF dust and coal can be described by the following reactions: (1) direct reduction (solid/solid) between iron oxides and carbon; and (2) gas/solid reactions. As the speed of solid/solid reaction is much slower than the gas/solid reaction, the global process occurs via gaseous intermediates such as $CO_{(g)}$, $CO_{2(g)}$, $H_{2(g)}$, and $H_2O_{(g)}$ [6]. Likewise, Kashiwaya et al. showed that the basic reaction mechanism of a composite pellet containing hematite and graphite starts at ~923 K as a reaction caused by the direct contact between iron oxide and carbon and then, after subsequent separation of the iron oxide/carbon interface, the reaction continues as a coupling

phenomenon between reduction and carbon gasification [7]. Reduction can start at even lower temperatures in the event of gas generation in the solid due to decomposition and/or volatilization. Mookherjee et al. observed that the volatile matter in non-coking coal contributed to the reduction of iron ore at temperatures over 773 K [8]. Furthermore, Lu et al. showed that volatile matter in coal contributed to the reduction of iron oxide and was effectively consumed in the process and direct contact of iron ore fines and coal fines increased the reduction rate in the *prereduction* stage of their experimental furnace [9, 10].

Various studies have been found in the literature concerning gasification of carbonaceous material in the presence of different metal-based sorbents/catalysts, mostly at elevated pressure ~20 MPa [11–13]. Results from Sato et al. have shown that water contained in $Ca(OH)_2$ molecules is sufficient to produce $H_{2(g)}$ from reaction with carbon content in samples of a vacuum reside of Arabian light crude oil at temperatures above 873 K and pressures 4–5 MPa [14].

Some critical reactions that are relevant for conditions occurring in cold-bonded pellet samples during heat treatment in inert gas have been found in the literature. These reactions are defined as metal oxide dehydration, the steam–carbon reaction and/or water–gas shift reaction, the Boudouard reaction and subsequent reduction of iron oxide through its reaction with gaseous reductants generated from former reactions [15]. Earlier results from the current authors [16], have shown evidence of carbon gasification (small amounts of $CH_{4(g)}$ and $H_{2(g)}$ generation) during the decomposition of $Ca(OH)_2$, in the presence of graphite, between 573 and 1,073 K in inert atmosphere.

Therefore, the objective of the present work is to study the mechanisms of reaction in the $Ca(OH)_2$–C–Fe_2O_3 system at temperatures below 1,073 K and at ambient pressure. The reactions of most importance to this study are listed below:

$$Ca(OH)_2 = CaO + H_2O \quad (1)$$

$$C/CO + H_2O = CO/CO_2 + H_2 \quad (2)$$

$$CO_2 + C = 2CO \quad (3)$$

$$Fe_xO_y + C/CO/H_2 = Fe_xO_{y-1} + CO/CO_2/H_2O \quad (4)$$

$$2CaO + Fe_2O_3 = Ca_2Fe_2O_5 \quad (5)$$

Experimental

Materials

The raw materials used in this study are all laboratory grade reagents. Calcium hydroxide, 99.8% pure powder, was supplied from Riedel–deHaen; standard Hematite, 99.8%(metals basis) pure and −325 mesh powder, was supplied from Alfa Aesar; Graphite, 99% pure and −300 mesh, was supplied from Alfa Aesar. Micro briquettes were prepared from the reagent powder mixtures in a hand press, 1.5 N/mm^2, resulting in cylinders having average dimensions of 3 mm $\phi \times 3$ mm H and sample mass of 15.7 ± 2.3 mg. The particle size distributions of the standard-sized reagents are given in Fig. 1. The reagent mixture composition used during experimental work, shown in Table 1, is based on relative compositions between the three reagents in industrial cold-bonded agglomerates from an earlier study [4].

In order to study the influence of particle size on the transformations occurring in the $Ca(OH)_2$–C–Fe_2O_3 system, a finer Fe_2O_3 particle size was used for sample 2 as shown in Table 1. The nano-sized Hematite, 99.999% pure powder with an average size of 30 nm, was also supplied from Aldrich. Again, micro briquettes were prepared using the same method mentioned earlier resulting in an average sample mass of 18 ± 1 mg.

Methods

A Setaram Setsys Evolution instrument equipped with simultaneous thermo-gravimetric (TG), differential thermal (DTA), and quadrupole mass spectrometric (QMS) analysis was used in thermal analysis studies. The sensitivity of the TG balance is ±0.3 μg.

In order to investigate the influence of heating rate, TG/DTA/QMS tests were conducted on both samples shown in Table 1 using heating from 293 to 1,073 K at either 2, 10, or 32 K/min in helium with a constant flow rate of 60 ml/min. Cylindrical α-Al_2O_3 crucibles with a diameter of

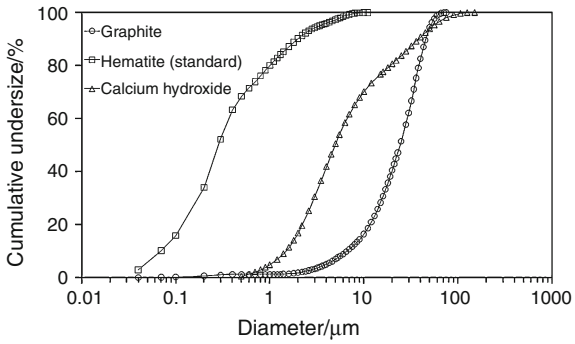

Fig. 1 Particle size distribution of the reagents

Table 1 Sample compositions in mass/%

Samples	$Ca(OH)_2$	C	Standard Fe_2O_3	Nano Fe_2O_3
1	25	12.5	62.5	
2	25	12.5		62.5

4 mm and a capacity of 100 µl were used in these tests. Select samples have been analyzed using a Siemens D5000 X-ray powder diffractometer using Ni-filtered Cu K_α radiation at 40 kV and 50 mA as well as scanning electron microscope investigation using a Philips XL 30.

Kinetic analysis

TG results from experiments have been studied using the Netzsch Thermokinetic software package [17]. In the kinetic analysis, TG results have been expressed as reaction extent α,

$$\alpha = (W_i - W)/(W_i - W_f) \quad (6)$$

where W is the mass or wt% of the sample at a given time, and W_i and W_f are the initial and final values for the transformation.

A multi-curve method has been applied to the non-isothermal measurements of each sample, specifically the Friedman iso-conversion method. Friedman analysis is based on the Arrhenius equation in a form shown here in Eq. 7:

$$\ln(d\alpha/dt) = \ln(A/f(\alpha)) - E/RT \quad (7)$$

The software provides values for the activation energy, E, and the natural logarithm of the pre-exponential factor, ln A. This analysis has been used as a precursor to linear and non-linear regression parts of the kinetic analysis software in order to estimate the magnitude of activation energy in correlation to conversion degree and temperature. In the multiple linear regression section, a series of experimental data was fit to a variety of different kinetic models for a one-step process. Based on results from Friedman analysis and multiple linear regression, multivariate non-linear regression was used to fit TG data to multi-step consecutive processes with the goal of outlining reaction mechanisms of the system $Ca(OH)_2$–C–Fe_2O_3 within the temperature range of 573–1,073 K. The derivative, $f(\alpha)$, and integral, $g(\alpha)$, kinetic model functions in the Arrhenius rate equation appearing in this study are summarized in Table 2.

Results and discussion

TG/DTA/QMS results

Thermal analysis was performed on micro briquettes of samples 1 and 2 to investigate the kinetic effect of heating rate and hematite grain size. Three heating rates have been used; 2, 10, and 32 K/min. As mentioned earlier, two different average grain sizes for reagent hematite have been used, ~300 nm (standard) and ~30 nm (nano). TG, DTA, and QMS results are shown for sample 1 and 2 in Fig. 2.

TG results reveal clear differences in mass loss behavior between the two samples. First, there is a difference in total mass loss between sample 1, ~10 mass/%, and sample 2, ~8 mass/%. Second, the fraction of total mass loss for the two separate TG steps (see temperature intervals in Table 3) in each sample differs, i.e. sample 1 (step 1 ≈ 0.3, step 2 ≈ 0.7) and sample 2 (step 1 ≈ 0.75, step 2 ≈ 0.25).

DTA results complement TG results where the heat flow during step 1 is roughly two times greater for sample 2 than that sample 1. Furthermore, the heat flow during step 2 is roughly 3.5 times greater for sample 1 than that sample 2. Interestingly, a difference does occur between heating rates where both samples exhibit small amounts of exothermic heat flow between 773 and 873 K when heated at 32 K/min, which otherwise was not observed at lower heating rates. The reduction of Fe_2O_3 by CO/H_2 in reaction 4 is mildly exothermic as well as carbon deposition by the reverse of reactions 2 or 3.

An example of the QMS curves for samples 1 and 2 are shown in Fig. 2. Obvious differences in evolved gas intensities, especially for H_2O and CO, correspond directly with mass loss results from both samples. For closer

Table 2 The derivative, $f(\alpha)$, and integral, $g(\alpha)$, kinetic model functions for the Arrhenius rate equation appearing in this study

Code	$g(\alpha)$	$f(\alpha)$	Kinetic model type
Fn	$(1/(1-\alpha)^{n-1}) - 1$	$(1-\alpha)^n$	nth order, $n \leq 3$
R2	$1-(1-\alpha)^{1/2}$	$2(1-\alpha)^{1/2}$	Two-dimensional phase boundary
R3	$1-(1-\alpha)^{1/3}$	$3(1-\alpha)^{2/3}$	Three-dimensional phase boundary
B1	$\ln(\alpha/(1-\alpha)) + c$	$(1-\alpha)\alpha$	Prout–Tompkins autocatalysis
An	$(-\ln(1-\alpha))^{1/n}$	$n(1-\alpha)[-\ln(1-\alpha)]^{(n-1)/n}$	Avrami–Erofeev nucleation/growth, n (reaction index) ≤4
D1	α^2	$1/2\alpha$	One-dimensional diffusion
D2	$\alpha + (1-\alpha)\ln(1-\alpha)$	$-1/\ln(1-\alpha)$	Two-dimensional diffusion
D3	$[1-(1-\alpha)^{1/3}]^2$	$[3(1-\alpha)^{2/3}]/[2[1-(1-\alpha)^{1/3}]]$	Three-dimensional diffusion

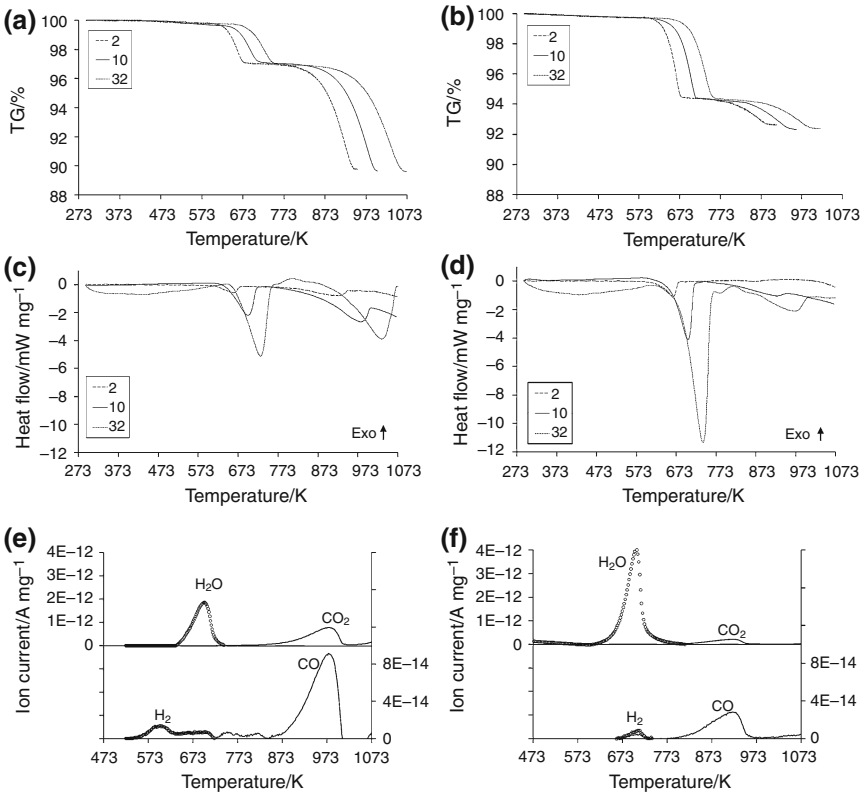

Fig. 2 TG results from **a** sample 1 and **b** sample 2 at different heating rates. DTA results from **c** sample 1 and **d** sample 2 at different heating rates. QMS curves from **e** sample 1 and **f** sample 2 heated at 10 K/min

Table 3 Upper part: temperature interval definitions for each TG step in both samples 1 & 2 Lower part: Average calculated response for TG step 2 in samples 1 & 2

β/K min^{-1}	ΔT/K	
	Step 1	Step 2
2	593–703	723–953
10	613–743	773–1013
32	643–783	813–1073

Samples	RD_{app}/%	η_{H_2O}/%	η_{CO}/%
1	25.2	51.1	86.9
2	7.5	6.0	73.5

analysis, mass loss and maximum gas intensity data during step 2 has been used to calculate apparent reduction degree (RD_{app}), H_2O utilization degree (η_{H_2O}) following dehydration of $Ca(OH)_2$ content, and CO utilization degree (η_{CO}) in reduction reactions. The lower part of Table 3 shows a clear difference between η_{H_2O} of samples 1 and 2 having a marked negative effect on the calculated reduction degree of sample 2.

SEM results of raw and heat treated samples

Figure 3 shows cross sections of micro briquettes of sample 1 heated to 1,073 K. Figure 3a shows the outer edge of a sample heated at 2 K/min. In this sample, CaO particles are intact and porous indicating that little structural change has occurred in the grain after dehydration. From EDS results, we observed that iron oxide particles have an average iron content lying between magnetite and wustite. Figure 3b shows a large iron oxide particle or sintered grouping of many particles after heating at 10 K/min. Here, we observed a reduction gradient where points 1 & 3 have iron content close to magnetite and 2 & 4 hematite. In Fig. 3c, a particle of calcium-rich calcium ferrite seemingly has started to crystallize and become more angular in shape. The reduction degree of iron oxide in sample 1 did increase slightly with an increase in heating rate. Evidence of hematite reduction and calcium ferrite formation has been verified by powder XRD of sample 1 after heat treatment to 1,073 K, see Fig. 4.

SEM results from tests with sample 2 are given in Fig. 5. Figure 5a shows an example of crack formation in a micro briquette of sample 2 heated at 10 K/min. This behavior was observed in all trials with sample 2 independent of heating rate but was more prevalent at 10 and 32 K/min. In Fig. 5b, we observed a higher degree of reduction in iron oxide grain 2 (semi reduced FeO/Fe) and 3 (FeO) than in sample 1. This behavior was not seen throughout the entire micro briquette but in specific areas with a high local concentration of graphite in contact with iron oxide. Grain 1 shows an example of calcium ferrite with a gradient between Ca and Fe content. In Fig. 5c, we

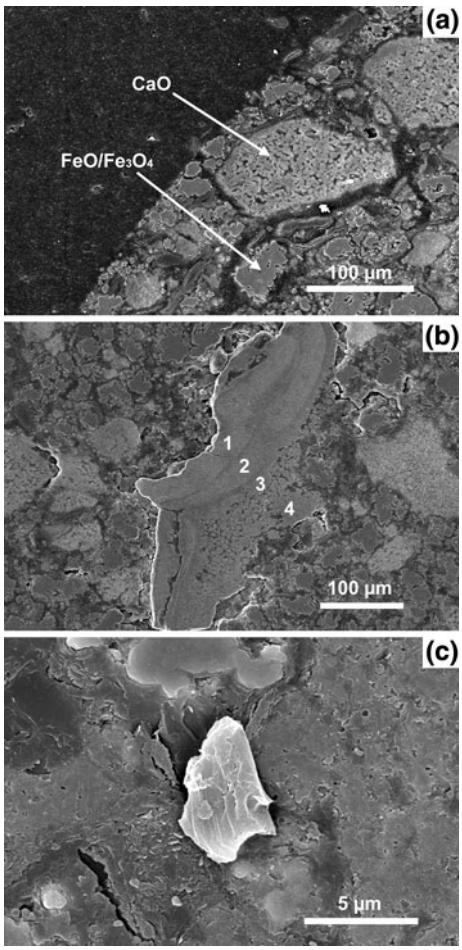

Fig. 3 SEM cross sections of heat treated sample 1 at **a** 2 K/min, **b** 10 K/min, **c** 32 K/min

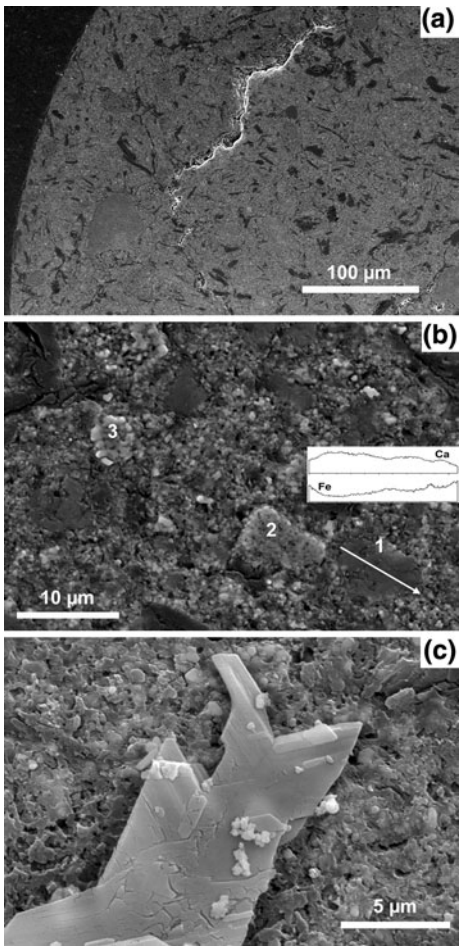

Fig. 5 SEM cross sections of heat-treated sample 2 at **a** 2 K/min, **b** 10 K/min, **c** 32 K/min

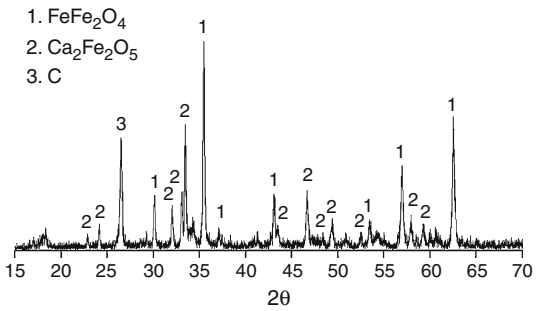

Fig. 4 XRD of sample 1 heat treated to 1,073 K

observed a highly crystallized grain of calcium ferrite in the middle of a sample heated at 32 K/min.

Kinetic results

Friedman analysis and master plots

Diagrams illustrating the model-free Friedman analysis of the TG results from samples 1 & 2 are shown in Fig. 6. The TG results have been treated as two step transformations in both samples for ease of evaluation. The main differences between the two samples is first, the dissimilarity between the trend in apparent activation energy at conversions of $\alpha > 0.9$ in step 1, i.e. Fig. 6a and c, and second, the increasing trend in activation energy at $\alpha > 0.9$ in step 2 for sample 2 but not for sample 1, Fig. 6b and d. Apart from these differences, both samples show similar dependence of the activation energy on conversion and this behavior is often a sign that each transition contains multiple steps [17].

In order to more closely evaluate the possible kinetic models that best describe the transformations occurring in samples 1 & 2, a "master plot" can be constructed to compare theoretical curves with the current experimental curves. This method allows the user to discern the predominant kinetic model or family of models that best match the experimental results using a relationship that is generally independent of the measured kinetic parameters. The specific master plot used here is based on the following function [18–20]:

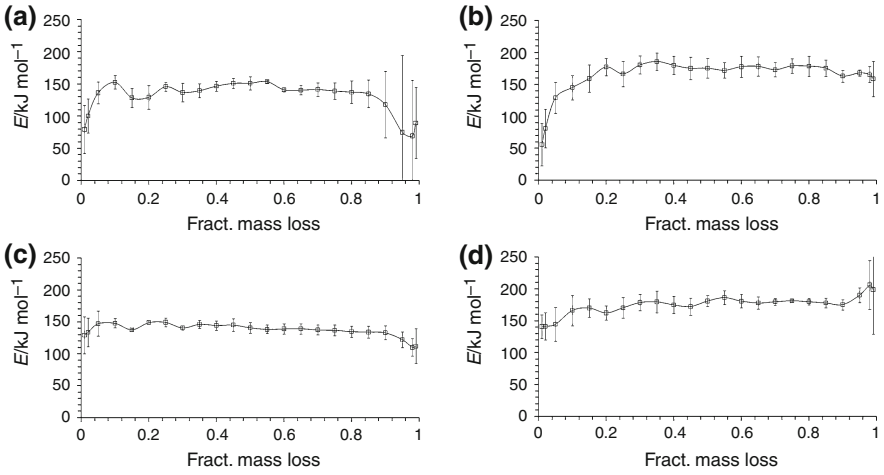

Fig. 6 Friedman analysis of sample 1, **a** TG step 1, **b** TG step 2 Friedman analysis of sample 2, **c** TG step 1, **d** TG step 2

$$Z(\alpha) = \frac{\mathrm{d}\alpha/\mathrm{d}t}{\beta}\mu(x)T \tag{8}$$

If we substitute the derivative and integral form of the Arrhenius rate equation into Eq. 8,

$$\mathrm{d}\alpha/\mathrm{d}t = Af(\alpha)\exp(-E/RT) \tag{9}$$

$$g(\alpha) = \frac{AE}{R\beta}\exp(-x)\frac{\mu(x)}{x} \tag{10}$$

where $x = E/RT$, $\beta = \mathrm{d}T/\mathrm{d}t$ and the fourth-degree rational approximation of the temperature integral taken from Senum and Yang [21]:

$$\mu(x) = \frac{x^3 + 18x^2 + 88x + 96}{x^4 + 20x^3 + 120x^2 + 240x + 120} \tag{11}$$

we arrive at the expression,

$$Z(\alpha) = f(\alpha)g(\alpha) \tag{12}$$

As seen in Fig. 7, the theoretical values of $Z(\alpha)$ for the most common kinetic model types have been plotted against α using Eq. 12 and expressions for $f(\alpha)$ and $g(\alpha)$ from Table 2. Experimental values of $Z(\alpha)$ have been plotted for samples 1 & 2 using Eqs. 8 and 11.

The experimental results for step 1 in sample 1, Fig. 7a, lie between An and Fn functions at conversions of $\alpha \leq 0.2$ with results from 2 K/min having a larger dimension/smaller order than results from 10 and 32 K/min. This behavior implies that the initial reaction mechanism is more reversible at lower heating rates. At higher degrees of conversion, $0.2 < \alpha \leq 0.8$, experimental results seem to follow a trend similar to that of the R2 kinetic model, and then follow the sharp negative slope of an An kinetic model near the end of conversion. Step 2, Fig. 7b, shows general agreement with the An/Fn curves at $\alpha \leq 0.3$ and then follows the R2 curve at greater conversion levels.

Master curve results for step 1 in sample 2, Fig. 7c, also seem to obey an An and/or Fn function throughout the entire conversion but at $0.6 \leq \alpha \leq 0.9$ results for 2 K/min deviate to a larger dimension/smaller order than do results from 10 and 32 °C/min. In step 2, Fig. 7d, experimental results are quite erratic but generally follow a trend comparable to An and/or Fn behavior at $\alpha \leq 0.4$ and then converge to a trend similar to R3 behavior at greater conversion levels. However, results from 2 and 10 K/min do show some adherence to D1, i.e. diffusion control, behavior at $0.5 \leq \alpha \leq 0.8$.

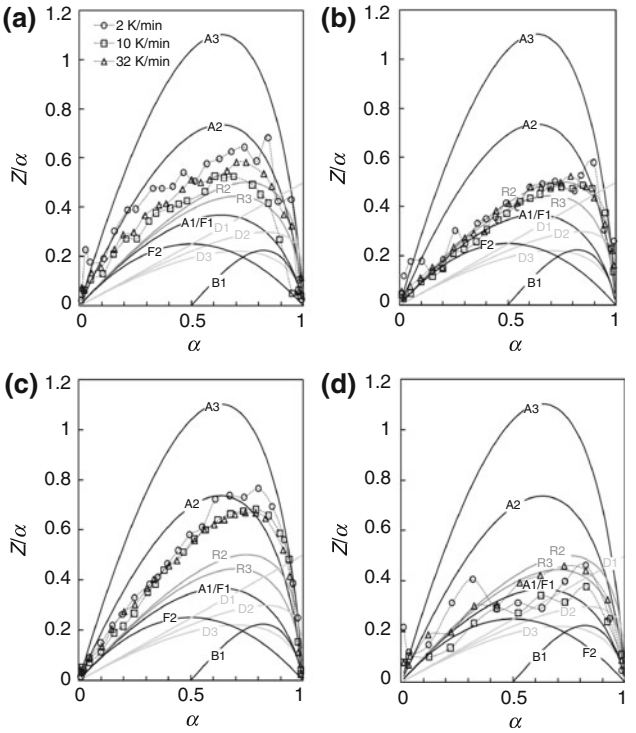

Fig. 7 $Z(\alpha)$ diagram for sample 1; **a** TG step 1, **b** TG step 2 $Z(\alpha)$ diagram for sample 2, **c** TG step 1, **d** TG step 2 (for definitions of kinetic model types see Table 2)

Non-linear regression analysis

With knowledge gained from Friedman and master plot analysis, configurations of consecutive and concurrent multiple reactions were tested in the non-linear regression analysis. Throughout the course of analysis, it became apparent that a concurrent configuration of multiple reactions was far inferior to consecutive reactions. This was evident due to relatively low correlation coefficients and very large standard errors returned by concurrent reaction models. Furthermore, TG and DTA results show very little if any significant dependence on the heating rate, which speaks against a branched/concurrent reaction path. With reservation for some overlapping between the start and finish of the proposed reaction models, a consecutive configuration of multiple reactions has been used in the current analysis. Results from the regression analysis of TG experiments involving sample 1 and sample 2 are shown in Table 4 and Fig. 8.

Sample 1

The initial Fn behavior in TG step 1 can be interpreted as a mechanism beginning with CaO product nuclei formation that is somewhat impeded by the reverse process of rehydration indicated by an order less than 1. Normally, CaO nuclei formation would be followed by the formation of a dense reaction layer [22], but because of the tightly packed multi-component structure in the micro briquettes gas diffusion is hindered thereby increasing the residence time of product H_2O gas allowing rehydration to occur.

The agreement with the R2 model at $0.19 < \alpha \leq 0.93$ can possibly be attributed to a reaction mechanism where advancement of the reaction interface is related to the layered crystal structure of $Ca(OH)_2$, i.e. if product nucleation occurs at the more-reactive edge surfaces of a plate-like crystal then the reaction layer would progress inwards two-dimensionally [23]. However, another possible explanation to this type of physico-geometric behavior was observed by Barret [24], where the characteristics of the phase-boundary reaction were shown to depend on the shape of the crucible, i.e. a cylindrical crucible results in R2 behavior. The activation energy for the R2 model is slightly higher than the energy for dehydration of $Ca(OH)_2$ found in literature, $\sim$120 kJ/mol. This can be due to overlap with subsequent Fn model behavior during the formation of $CO_{(g)}$ from graphite gasification. Activation energies for the steam–carbon reaction are of the magnitude 150 kJ/mol at atmospheric pressure but are highly dependent on the local steam partial pressure, temperature, and CO/CO_2 ratio [25].

The initial model behavior in TG step 2 is rationally tied to the end of TG step 1. Here, the An behavior ($\alpha < 0.24$) can be interpreted as random growth of the $CO_{2(g)}/Fe_3O_{4(s)}$ interface where CO_2 is a product from hematite reduction. Following interface growth, continuing reduction of hematite apparently proceeds via the phase-boundary mechanism, R2. El-Geassy's work also concludes this type of mixed reaction mechanism for the reduction of hematite [26]. The apparent activation energy from the model, $\sim$180 kJ/mol, lies in between energy values for gaseous reduction of iron oxide, 36–71 kJ/mol [27–29], and the intrinsic energy for the Boudouard reaction of approximately 400 kJ/mol [30]. This behavior, i.e. the reaction between solid carbon and iron oxide occurring as a combination of carbon gasification and carbothermic reduction, is generally accepted in the literature [31].

Table 4 Results of regression kinetic analysis

Sample 1: multivariate non-linear regression results						
TG step	Model	Order or dimension/*n*	w[a]	E_a/kJ mol^{-1}	ln A/s^{-1}	R^2
1	Fn	0.75	0.19	179.41 ± 3.99	27.26 ± 0.87	0.99950
	R2	2	0.74	148.63 ± 1.1	20.01 ± 0.18	
	Fn	0.79		126.05 ± 14.35	15.38 ± 1.49	
2	An	0.69	0.24	191.94 ± 5.51	19.25 ± 1.35	0.99921
	R2	2		178.79 ± 2.44	15.73 ± 0.23	
Sample 2: multivariate non-linear regression results						
TG step	Model	Order or dimension/*n*	w	E_a/kJ mol^{-1}	ln A/s^{-1}	R^2
1	Fn	0.54	0.37	153.83 ± 2.81	22.04 ± 0.67	0.99888
	An	1.46	0.29	140.32 ± 10.52	20.03 ± 1.84	
	An	2.12		139.97 ± 6.85	19.50 ± 1.08	
2	Fn	1.32	0.32	152.98 ± 3.92	16.03 ± 0.53	0.99775
	R3	3		188.42 ± 2.84	18.35 ± 0.39	

[a] Parameter w is a weighting factor used in multiple reaction models

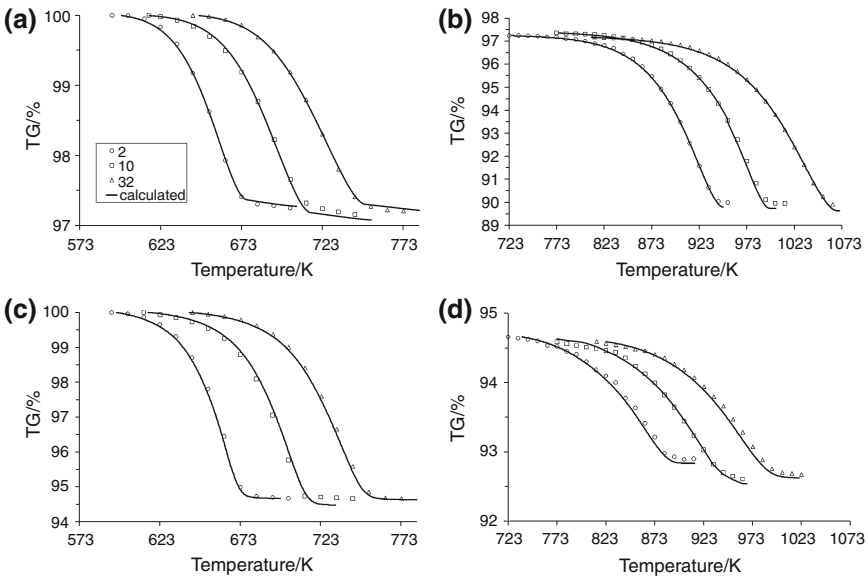

Fig. 8 Fit of the TG measurements using models in Table 4; sample 1 **a** TG step 1, **b** TG step 2 and sample 2 **c** TG step 1, **d** TG step 2

Sample 2

In sample 2, the initial Fn model in TG step 1 is similar to that in sample 1 but the order of reaction is lower. This is most likely due to the finer hematite grain size in sample 2 causing a decrease in total porosity within the briquette. Consequently, gas diffusion would become more difficult in the briquette thereby increasing the reversibility of the dehydration reaction in this initial stage. Next, in contrast to the behavior in sample 1, sample 2 follows nucleation/growth behavior during the 2nd stage rather than phase-boundary behavior. In reference to Fig. 2, the derivative of TG results show that the maximum rate of mass loss in step 1 for sample 2 ($\sim$1.4%/min) is more than twice that in sample 1 ($\sim$0.6%/min). An explanation can be that, instead of a slow advancement of the reaction interface as seen in sample 1, cracks develop in sample 2 due to excessive gas pressure build-up caused by overly dense particle packing resulting in more rapid and extensive dehydration. At the same time, the n exponent is close to 1.5, signifying that nucleation is instantaneous and growth of CaO occurs preferably in one direction more than the other [32]. The final stage of TG step 1 follows A2 behavior and can be interpreted as the growth of the $CO_{(g)}$/$C_{(s)}$ interface during graphite gasification. The gasification reaction can be starved due to low steam pressure, so the small amounts of $CO_{(g)}$ that are produced will more likely remain adsorbed to solid graphite surfaces [33] rather than participating in reduction reactions.

In TG step 2, the transition seems to initially follow Fn behavior interpreted as the direct reaction between $C_{(s)}$ and $Fe_2O_{3(s)}$ at those graphite surfaces which are in close contact with iron oxide. At lower heating rates (2 and 10 K/min), chemical control might be deferred by diffusion control as seen by the apparent correlation to D1 behavior in master curve analysis, Fig. 7d. Following initial direct reduction, further reduction of hematite apparently proceeds via phase-boundary mechanism, R3. The shrinking core model is more preferable in sample 2 than in sample 1 likely due to the much finer hematite particle size in sample 2 as well as the larger apparent activation energy, $\sim$190 kJ/mol, signifying more control by the Boudouard reaction, reaction 3.

Conclusions

The complex series of transformations occurring when iron and steelmaking by-product agglomerates are used as recycled iron charge in steelmaking processes was investigated on the basis of a simpler model system: Fe_2O_3–$Ca(OH)_2$–C in inert atmosphere.

The kinetics of two chemically identical samples, with two different grain sizes of hematite, was investigated. The overall transformation below 1,073 K involves a series of reactions, including calcium hydroxide dehydration, carbon gasification, iron oxide reduction, and calcium ferrite formation.

With briquettes containing micro-sized hematite, the transformation starts with calcium hydroxide dehydration, whose first step, CaO nucleation, is somewhat impeded by the slow escape of H_2O imposed by the tight structure of the briquette. Dehydration proceeds by the inward 2D growth of the CaO grains. Evolved steam in turn begins gasifying carbon grains, producing CO and H_2. Then, the reduction of hematite takes place by these gases, also via a 2D phase-boundary mechanism, to a reduction degree between magnetite and wustite. Parallel to the iron oxide

reduction, a calcium ferrite phase appears, in the form of angular and calcium-rich particles.

In the case of briquettes containing nano-sized hematite, the course of the transformation is slightly different. Nucleation of CaO starts more slowly due to lower total porosity of the briquette, but soon after, the development of cracks, which is favored by high heating rates, makes dehydration more rapid and more extensive. Carbon gasification by steam is hampered by lower water pressures after crack formation. Locally, where hematite grains are in close contact with carbon particles, direct reduction can occur followed by a 3D phase-boundary mechanism resulting in select iron oxide grains reaching a reduction degree equivalent to wustite.

Acknowledgements The authors would like to express their gratitude to Mr. Bernard Rouat for all help in laboratory and the Foundation of King Carl XVI Gustaf's 50th Birthday Fund for financial support during the completion of this work.

References

1. Takano C, Nascimento RC, Silva GFBL, dos Santos DM, Mourao MB. Recycling of solid wastes containing iron from integrated steelmaking plant. In: EPD congress; 2001, TMS, p. 183–193.
2. Gudenau HW, Senk D, Wang S, De Melo Martins K, Stephany C. Research in the reduction of iron ore agglomerates including coal and C containing dust. ISIJ Int. 2005;45(4):603–8.
3. Ahn JS, Chon CM, Moon HS, Kim KW. Arsenic removal using steel manufacturing byproducts as permeable reactive materials in mine tailing containment system. Water Res. 2003;37(10): 2478–88.
4. Robinson R. High temperature properties of by-product cold bonded pellets containing blast furnace flue dust. Thermochim Acta. 2005;432:112–23.
5. Takano C, Mourao MB. Self-reducing pellets for ironmaking: mechanical behavior. Miner Processing Extr Metall Rev. 2003; 24:233–52.
6. Mantovani MC, Takano C. The strength and high temperature behaviors of self-reducing pellets containing EAF dust. ISIJ Int. 2000;40(3):224–30.
7. Kashiwaya Y, Kanbe M, Shii K. Reaction behavior of facing pair between hematite and graphite: a coupling phenomenon of reduction and gasification. ISIJ Int. 2001;41:818.
8. Mookherjee S, Ray HS, Mukhrjee A. Isothermal reduction of iron ore fines surrounded by coal och char fines. Ironmaking Steelmaking 1986;13:229–35.
9. Lu W-K, Bryk C, Gou H. The LB furnace for smelting reduction of iron ore. In: Proceedings of the 5th international iron and steel congress, Book 3, vol 6. 1986, p. 1065–1075.
10. Gou H, Lu W-K, Bryk C. Bench scale test of a new ironmaking process with mixture of iron ore concentrate and pulverized coal. ISIJ Int. 1992;32:733–40.
11. Kumabe K, Moritomi H, Yoshiie R, Kambara S, Kuramoto K, Suzuki Y, Hatano H, Lin SY, Harada M. Gasification of organic waste with subcritical steam under the presence of a calcium-based carbon dioxide sorbent. Ind Eng Chem Res. 2004;43: 6943–7.
12. Wang J, Takarada T. Role of calcium hydroxide in supercritical water gasification of low-rank coal. Energy Fuels. 2001;15: \356–62.
13. Inui T, Otowa T, Okazumi F. Gasification of active carbon by iron-based composite catalysts for obtaining directly a gas of optional H_2/CO ratio. Carbon. 1985;23(2):193–208.
14. Sato S, Lin SY, Suzuki Y, Hatano H. Hydrogen production from heavy oil in the presence of calcium hydroxide. Fuel. 2003;82: 561–7.
15. Sohn HY, Wadsworth EM. Rate processes of extractive metallurgy. New York: Plenum Press; 1979.
16. Robinson R, Menad N, Björkman B. Low temperature behavior of the $Ca(OH)_2$–C system and its significance on the self-reduction of cold bonded by-product agglomerates. In: Proceedings of the 4th ICSTI. 2006, p. 311–314.
17. Opfermann J. Kinetic analysis using multivariate non-linear regression. I. Basic concepts. J Therm Anal Calorim. 2000;60: 641–58.
18. Ortega A. The kinetics of solid-state reactions toward consensus, Part 2: fitting kinetic data in dynamic conventional thermal analysis. Int J Chem Kinetics. 2002;34:193–208.
19. Koga N, Sestak J, Malek J. Distortion of the Arrhenius parameters by the inappropriate kinetic model function. Thermochim Acta. 1991;188:333.
20. Criado JM, Ortega A, Gotor F. Correlation between the shape of controlled rate thermal analysis curves and the kinetics of solid state reactions. Thermochim Acta. 1990;157:171–9.
21. Senum GI, Yang RT. Rational approximations of the integral of the Arrhenius function. J Therm Anal. 1977;11:445–7.
22. Galwey AK, Laverty GM. A kinetic and mechanistic study of the dehydroxylation of calcium hydroxide. Thermochim Acta. 1993;228:359–78.
23. Koga N, Tanaka H. A physico-geometric approach to the kinetics of solid-state reactions as exemplified by the thermal dehydration and decomposition of inorganic solids. Thermochim Acta. 2002; 388:41–61.
24. Barret P. In: International proceedings of the 4th symposium on the reactivity of solids. 1960, p. 178.
25. Mann MD, Knutson RZ, Erjavec J, Jacobsen JP. Modelling reaction kinetics of steam gasification for a transport gasifier. Fuel. 2004;83:1643–50.
26. El-Geassy AHA. Stepwise reduction of CaO and/or MgO doped-Fe_2O_3 compacts (hematite-wustite-iron transformation steps). Scandinavian J Metall. 1998;27:205.
27. Turkdogan ET. Reduction of iron oxides. In: 31st Ironmaking conference proceedings. 1972, p. 438–458.
28. Turkdogan ET, Vinters JV. Gaseous reduction of iron oxides: Part I. Reduction of hematite in hydrogen. Metall Mater Trans B. 1971;2(11):3175–88.
29. Dutta SK, Ghosh A. Kinetics of gaseous reduction of iron ore fines. ISIJ Int. 1993;33:1168–73.
30. Fortini OM, Fruehan RJ. Rate of reduction of ore-carbon composites: Part II. Modeling of reduction in extended composites. Metall Mater Trans B. 2005;36(B):709–17.
31. Haque R, Ray HS. Role of ore/carbon contact and direct reduction in the reduction of iron oxide by carbon. Metall Mater Trans B. 1995;26(B):400–1.
32. Malek J. The applicability of Johnson–Mehl–Avrami model in the thermal analysis of the crystallization kinetics of glasses. Thermochim Acta. 1995;267:61–73.
33. Turkdogan ET, Vinters JV. Effect of carbon monoxide on the rate of oxidation of charcoal, graphite and coke in carbon dioxide. Carbon. 1970;8:39–53.